The X-Point radiating regime at ASDEX Upgrade and TCV

M. Bernert[a,*], S. Wiesen[b], O. Février[c], A. Kallenbach[a], J.T.W. Koenders[d,e], B. Sieglin[a], U. Stroth[a,f], T.O.S.J. Bosman[d,e], D. Brida[a], M. Cavedon[a,g], P. David[a], M.G. Dunne[a], S. Henderson[h], B. Kool[d,e], T. Lunt[a], R.M. McDermott[a], O. Pan[a], A. Perek[c], H. Reimerdes[c], U. Sheikh[c], C. Theiler[c], M. van Berkel[d], T. Wijkamp[d,i], M. Wischmeier[a], the EUROfusion MST1 team[1], the TCV team[2], the ASDEX Upgrade team[3]

[a] *Max Planck Institute for Plasma Physics, Boltzmannstr. 2, 85748 Garching, Germany*
[b] *Forschungszentrum Jülich GmbH, Institut für Energie- und Klimaforschung - Plasmaphysik, 52425 Jülich, Germany*
[c] *EPFL, Swiss Plasma Center (SPC), CH-1015 Lausanne, Switzerland*
[d] *DIFFER - Dutch Institute for Fundamental Energy Research, De Zaale 20, 5612 AJ Eindhoven, Netherlands*
[e] *Department of Mechanical Engineering, CST Group, Eindhoven University of Technology, Eindhoven, Netherlands*
[f] *Physik-Department E28, Technische Universiät München, 85748 Garching, Germany*
[g] *Dipartimento di Fisica "G. Occhialini", Università di Milano-Bicocca, Milano, Italy*
[h] *CCFE, Culham Science Centre, Abingdon OX14 3DB, UK*
[i] *Department of Applied Physics, Eindhoven University of Technology, Eindhoven, Netherlands*

Abstract

Future fusion reactors require a safe, steady-state divertor operation. With deep divertor detachment, which is typically induced by impurity seeding, the radiation concentrates in a small region at the X-point or on closed flux surfaces above the X-point. This so-called X-point radiator (XPR) moves further inside the confined region with increasing seeding and the location can be actively controlled.

At AUG, the parameter space for operation with an XPR was significantly extended, using active feedback on the XPR location. The XPR is observed in nearly the whole operational space of AUG in the high-densities or high collisionality regime. ELM suppression is consistently observed in all cases where the XPR was moved to a significant height above the X-point.

Direct measurements of density and temperature from the region around the XPR using the new divertor Thomson scattering system at AUG indicate that the temperature at the location of the XPR remains high ($> 30eV$) and only cools down further towards the X-point. In this cold XPR core, the temperature reduces to about $1\,eV$.

An XPR is also observed in TCV by the injection of nitrogen as extrinsic impurity. This highlights that the wall material (W for AUG, C for TCV) or machine size does not play a significant role for the existence of the regime. However, the scenario appears to be less stable in TCV. First experiments show the necessity of an active control for the XPR: Depending on the wall conditions and the nitrogen wall storage, the required nitrogen seeding level to achieve an XPR changes.

Both, the low temperatures measured radially outside of the radiation zone at AUG, and the lower stability of the XPR regime at TCV with the presence of carbon are consistent with the predictions of a one-dimensional model of the XPR. However, the model would predict the development of the cold XPR

*Corresponding author, *E-mail address: matthias.bernert@ipp.mpg.de*
[1] See author list of "B. Labit et al 2019 Nucl. Fusion 59 086020"
[2] See author list of "H. Reimerdes et al 2022 Nucl. Fusion 62 042018"
[3] See author list of "U. Stroth et al. 2022 Nucl. Fusion 62 042006"

core, and significant radiation at the X-point might already exist before reaching this cold temperature solution.

---

1. Introduction

At ASDEX Upgrade (AUG) and JET H-mode discharges, with impurity induced divertor detachment, the radiation concentrates in a small region close to the X-point, inside the confined region. Figure 1 shows a camera image in the visible range of an AUG discharge with a so-called X-point radiator (XPR). This XPR can be generated with nitrogen or argon seeding at AUG, or also additionally with neon or krypton seeding at JET [1]. The location of the radiator relative to the X-point can actively be influenced and controlled in real-time by impurity seeding [2]. In TCV, an XPR was so far only observed in L-mode [3].

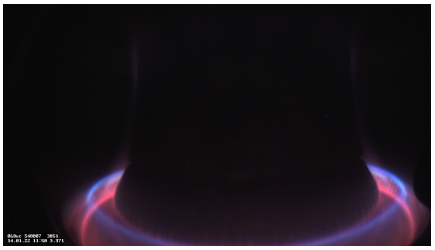

Figure 1: Visible camera image of a discharge with an XPR (AUG #40007, 3.4s) seen in blue light emitted by nitrogen, dominated by N^{2+}. Magenta is the typical Balmer emission from deuterium in a divertor leg.

An XPR is very similar or identical to an X-point MARFE [4], however, a MARFE is usually associated with a degradation of confinement or even an H-L back transition and the initialization of a disruption [5]. An X-point MARFE is mainly observed in L-mode discharges in many devices [6, 7, 8] and is correlated to the density limit [9]. In order to distinguish the stable radiation at the X-point from the non-stationary evolution of an X-point MARFE, the stable case is named here XPR. This XPR is also observed in H-mode and exists inside the confined region, close to or on the X-point. As soon as this radiation becomes non-stationary and moves up along the high field side, it is named MARFE, following the definition in [10]. An XPR can, however, by definition still be interpreted as an X-point MARFE.

It is possible to reproduce the radiation condensation, which is the thermal instability triggering the XPR or MARFE, with analytic calculations [4] and SOLPS modelling [11, 12, 13, 14]. In order to derive the main parameter dependencies for the access and stability conditions for an XPR, a model based on a one-dimensional power balance was recently developed [10]. Following this model, the presence of carbon (intrinsic for a carbon-walled device such as TCV) does not lead to a stable XPR, but would immediately develop into a MARFE, initiating a disruption. The observation of an XPR at TCV is challenging the one-dimensional model. In this work, XPRs in H-mode plasmas in TCV are presented and compared to the model.

In section 2, the operational range at AUG for the existence of an XPR with ELM suppression is discussed. The local measurements by the divertor Thomson scattering diagnostic will be compared with the 1D model. Section 3 demonstrates the existence of XPRs for H-mode scenarios at TCV, which is then further discussed in section 4.

2. Operational range and local parameters of an XPR at AUG

At AUG, in H-mode plasmas an XPR can be created by extensive impurity seeding. The standard seed impurity used is nitrogen, but also argon has been demonstrated. Real-time feedback control is implemented to steer the location of the radiator relative to the X-point, using impurity seeding as an actuator. [2]. This control scheme was further optimised and is now also set up for argon seeding, where the position of the XPR is much more sensitive on the seeding level due to the high radiation efficiency of argon.

Parameter	XPR existence	ELM suppression
I_P	0.8 - 1.2 MA	0.8 - 1.2 MA
B_t	1.8 & 2.5 T	1.8 & 2.5 T
q_{95}	3.7 - 6	3.7 - 6
P_{heat}	1.7 - 26 MW	1.7 - 17.5 MW
H_{98}	0.8 - 1.1	0.7 - 1
f_{GW}	0.7 - 0.95	0.7 - 0.8

Table 1: Parameter range of AUG, where the XPR is observed with N_2 seeding and where the ELM suppression was achieved

The operational range at AUG, where an XPR is observed with nitrogen seeding, was significantly extended in terms of I_P, B_t, q_{95} & P_{heat} compared to previous publications [2]. Table 1 lists the parameter range, where the XPR scenario was tested and accessed. In almost the complete operational range of AUG at high density or high collisionality the XPR was observed after the injection of a sufficient amount of nitrogen. The nitrogen concentration inside the confined plasma, measured by CXRS [15], is for such scenarios typically around $2-3\,\%$. ELM suppression is accessed when the XPR is significantly above the X-point (typically above $7cm$). Only at the highest heating powers it was not attempted to achieve the ELM suppression, therefore, the existence of this regime is only tested for up to $17.5\,MW$.

With the ELM suppression, the line averaged electron density and energy confinement decrease. The pedestal gradients are reduced, leading to lower pedestal top values. Since the electron temperature gradient further inwards is increased, the overall reduction in energy confinement is not very strong (about 10-15 %), while the reduction of the line averaged density is of the order of 20 %. The influence on the pedestal is discussed more in [2].

The divertor Thomson scattering system (DTS, [16]) allows direct measurements of electron density (n_e) and temperature (T_e) in the X-point region. Figure 2 shows the measurement location of DTS and the location of the XPR as identified by the AXUV diagnostic. The temperature at the location of the XPR remains high ($> 30eV$) at 2.5 s and only cools down further towards the X-point (see 3.25 s & 4.0 s). In this cold XPR core, the temperature reduces to the range of about $1\,eV$, below which the deuterium 3-body recombination rate strongly increases [17]. The strong density increase shows that the pressure conservation along the flux surface is maintained [18].

These findings are consistent with recent SOLPS-ITER simulations [14] which show that a fully developed XPR consists of a cold core close to the X-point surrounded by a radiating mantle. The spatial coverage and resolution of the DTS does not allow to identify if a (small) cold XPR core exists always as soon as the radiator is present.

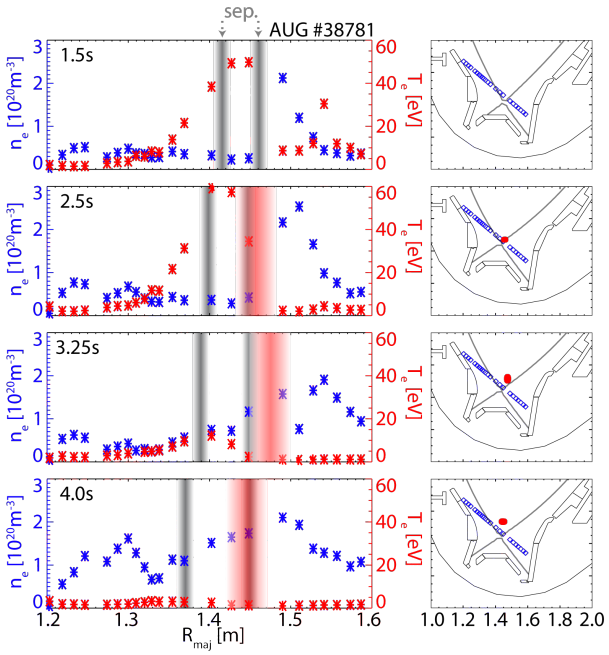

Figure 2: T_e and n_e from DTS at different time points in AUG #38781. The grey shaded areas indicate intersection of the DTS beam path with the separatrix, the red shaded area the radial location and width of the XPR (note: the XPR might be vertically higher than the DTS measurement location, thus, these measurements are located between the XPR and the separatrix). Right: Location and extend (FWHM) of the XPR (red) and the location of the DTS measurements (blue).

3. XPRs in H-mode at TCV

In TCV, XPRs have, until this study, only been determined to exist in L-mode plasmas [3]. In the following evidence is shown that the XPR also forms in TCV H-mode plasmas. The characteristics of those discharges is the following: ($I_P = -210\,kA$, $B_t = -1.4\,T$, $P_{heat} = 1.3\,MW$ (NBI)) in a conventional divertor configuration with nitrogen seeding ramps.

3.1. XPR observation in TCV

Figure 3 shows the shift of radiation with two pulses of nitrogen seeding, as observed by the AXUV cameras. Figure 4 shows that this shift is from the scrape-off layer (SOL), close to the X-point and inner

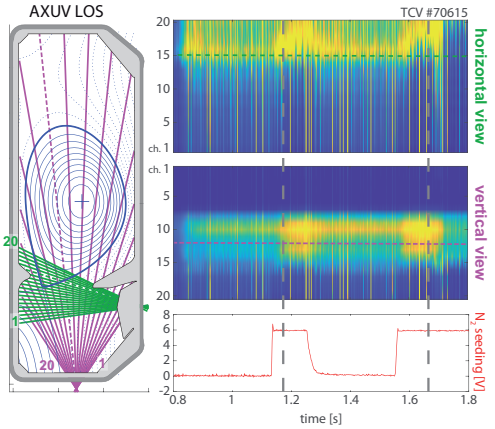

Figure 3: Left: LOS location of AXUV channels. Right: Contour plot of the measured intensity of the AXUV cameras from the side (top) and from below (middle), showing the shift of radiation depending on the nitrogen seeding rate (bottom). The most significant LOS are indicated by the dashed lines, the vertical grey lines indicate time points shown in figure 4.

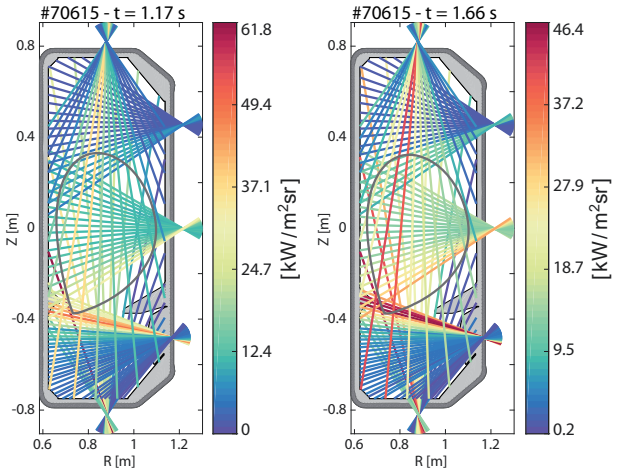

Figure 4: Bolometry line of sight intensity before and after creation of XPR in TCV #70615. The peak of radiation moves from outside (left) to inside the confined region (right).

baffle, to inside the confined region, indicating that an XPR was formed and moved for a few cm inside the confined region.

This concentration of the radiation inside the confined region can also be observed using the multi-spectral imaging diagnostic MANTIS [19], see figure 5. The N II emission is first distributed in the SOL, but later concentrates at the X-point. The emission of N II spectral lines is an indication of electron temperatures below $10\,eV$ (e.g. $6.5\,eV$ at the emission front [20]) in this region.

The shift of radiation inside the confined region, and with this the existence of the XPR, was observed in several discharges with different seeding trajectories. Figure 6 gives an overview of different trajectories applied. The location of the N II emission ($\lambda = 399.0nm$) peak is tracked using the MANTIS system, given in the coordinate L_{pol} (poloidal length along the divertor leg, $0\,m$ at the divertor target and $0.4\,m$ at the X-point). The range of the XPR regime in this measurement can be identified in accordance with other diagnostics and is color coded in the figure. Below $40\,cm$, the radiation is in the SOL, for $40 - 43\,cm$, the XPR is present. If the emission peak is detected higher, the plasma transits into L-mode and, if no fast countermeasure is taken, a radiative collapse and disruption follows.

The observations, e.g. in figure 6, indicate that the operational window for a stable XPR is much smaller for TCV than for AUG. Over-seeding can easily occur at TCV and the plasma tends to transit to L-mode and disrupt. Whether the higher sensitivity to seeding leading to the H-L transition and disruption in TCV compared to AUG is due to the differences in machine size, available heating power or the carbon wall cannot be concluded.

The 1D-model [10] predicts a lower stability for TCV: An XPR will convert to a non-stationary MARFE when the dominant radiating impurity is carbon, as it is intrinsic for TCV. However, seeing the existence of an XPR at TCV contradicts this prediction. But the model is not fully applicable if the XPR consists only of the radiating front but did not yet develop the cold core.

Furthermore, the operation at TCV is complicated by the unknown wall storage of nitrogen. Depending on the previous discharges and the discharge history, the same nitrogen seeding level might not be sufficient to create an XPR, or can lead to an over-seeding. In order to compensate for the unknown wall storage, an active control of the nitrogen seeding level is nec-

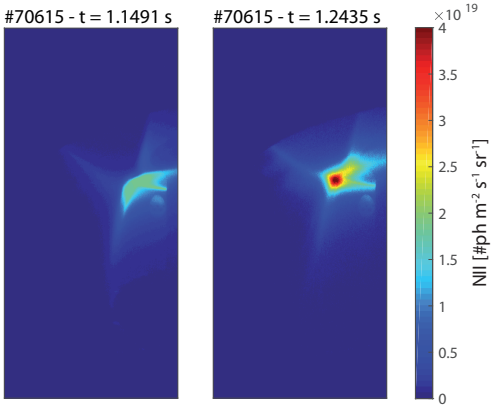

Figure 5: Filtered camera image of an N II spectral line (399.0 nm) by MANTIS before (left) and after (right) development of XPR in TCV #70615.

essary.

3.2. XPR controllability and active control at TCV

If the existence of radiation at the X-point immediately leads to a disruptive MARFE, the scenario would not be controllable. However, the plasma can recover from an XPR state, as seen in figures 3, 6 or 7, where the N II emission peak goes back to the target after switching off the seeding. Therefore, an active control might be possible.

The real-time front detection algorithm of [21] is adjusted to track the N II emission peak (location of the maximum emission) instead of the emission front (location where 50% of the peak signal are reached towards the target), once the N II emission front moves close to the X-point. This signal is used by a real-time controller in order to adjust the nitrogen seeding level to match the requested location of the emission peak. Figure 7 shows the comparison of a discharge with a feed forward programmed nitrogen seeding rate and one with successful active feedback.

In between ELMs, the noise of the peak tracking is within the camera resolution, in the range of 1 cm. The large peaks in the tracking signal are caused by ELMs, which lead to a strong emission at the divertor target, detected close to $L_{pol} = 0\,cm$. The disturbance of the real-time signal by the ELMs provokes a too high seeding rate (see Fig.7) and then causes a

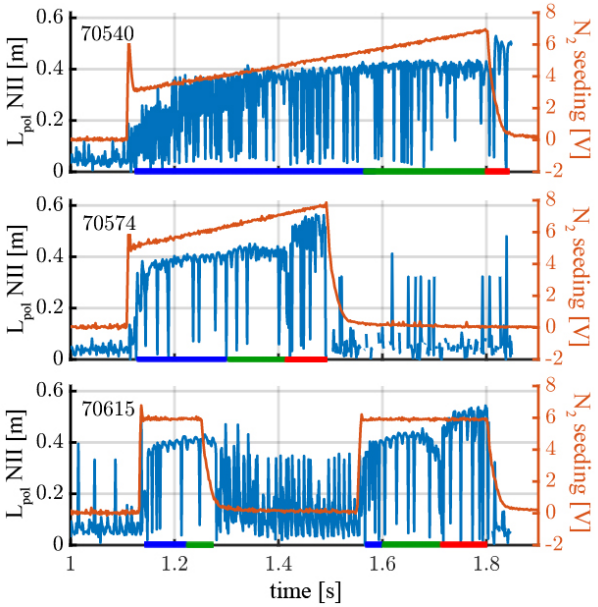

Figure 6: Nitrogen seeding level and N II emission peak position (vertical distance along the divertor leg, 0 m at the target, 0.4 m at the X-point) as tracked by the MANTIS system for three discharges at TCV. The large spikes are dominantly caused by ELMs. The colored bars along the time axes correspond to when the radiation is below the X-point (blue), the XPR exists (green) and the plasma transits back to L-mode (red).

radiative collapse. In order to avoid such errors, an ELM filter has to be applied to the real-time signal. This is yet to be done, as well as to extend the control to a broader range of scenarios.

4. Conclusion

Observing an X-point radiator at ASDEX Upgrade and TCV together with the observation at other devices (Alcator C-mod [6], JT-60U [7], JET [1]) shows that this feature is independent of the wall material or device size. For AUG, the operational range with an XPR is currently much broader than for TCV, covering almost the full available range of B_t, I_P and P_{heat}, while in TCV for now it is only tested in one specific scenario. For AUG, using the divertor Thomson scattering system one can observe a cold XPR core developing with a radiating mantle.

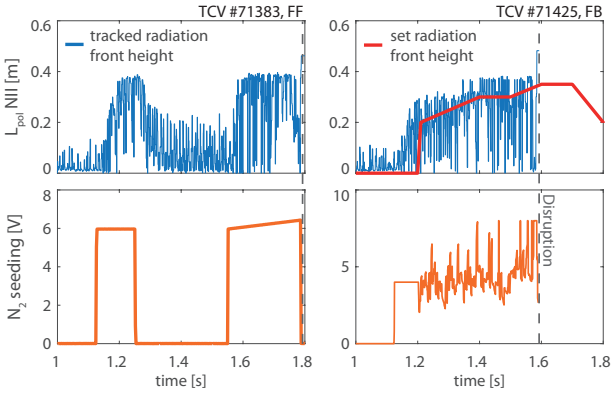

Figure 7: Tracked radiation peak height and nitrogen gas puff for a discharge with feed forward seeding (left) and with feedback on the radiation location (right). Note: Due to the operation in another campaign than Fig. 6, the range of the XPR regime in terms of L_{pol} is between $30 - 35\,cm$.

The one-dimensional model predicts that the plasma at the X-point transits from a high temperature ($T_{e,X} > 25\,eV$) to a low temperature solution ($T_{e,X} \leq 2\,eV$), which in the presence of carbon would be unstable [10]. These predictions appear to be in variance with the observation of an XPR at TCV. However, the model potentially only applies to the cold XPR core solution while in the case of TCV, the observed XPR might only be present by the radiation front, but did not yet develop the cold core. However, soon after the XPR develops into a non-stationary MARFE and disrupts. Therefore, the model might not be applicable for the onset of the radiation, but could well explain why the XPR cannot easily be maintained at TCV. Whereas at AUG, where carbon is not significantly present, the XPR is maintained also with the cold core and can be sustained for several seconds.

While X-point radiation is not the foreseen operational regime for the ITER divertor, the observation at multiple devices indicate that the XPR is a universal feature of tokamak plasmas and makes it a promising regime, which might also occur in future devices. In order to predict the access conditions and stability of an XPR for a reactor scale device, further experiments for a size scaling as well as significant modelling efforts are still required.

Acknowledgment

This work was supported in part by the Swiss National Science Foundation. This work has been carried out within the framework of the EUROfusion Consortium, funded by the European Union via the Euratom Research and Training Programme (Grant Agreement No 101052200 - EUROfusion). Views and opinions expressed are however those of the author(s) only and do not necessarily reflect those of the European Union or the European Commission. Neither the European Union nor the European Commission can be held responsible for them.

References

[1] M. Bernert, M. Wischmeier, A. Huber, F. Reimold, B. Lipschultz, C. Lowry, S. Brezinsek, R. Dux, T. Eich, A. Kallenbach, A. Lebschy, C. Maggi, R. McDermott, T. Pütterich, S. Wiesen, Power exhaust by SOL and pedestal radiation at ASDEX Upgrade and JET, Nuclear Materials and Energy 12 (2017) 111–118, proceedings of the 22nd International Conference on Plasma Surface Interactions 2016, 22nd PSI. doi:https://doi.org/10.1016/j.nme.2016.12.029.
URL https://www.sciencedirect.com/science/article/pii/S2352179116302174

[2] M. Bernert, F. Janky, B. Sieglin, A. Kallenbach, B. Lipschultz, F. Reimold, M. Wischmeier, M. Cavedon, P. David, M. Dunne, M. Griener, O. Kudlacek, R. McDermott, W. Treutterer, E. Wolfrum, D. Brida, O. Février, S. Henderson, M. Komm, EUROfusion MST1 team, and the ASDEX Upgrade team, X-point radiation, its control and an ELM suppressed radiating regime at the ASDEX Upgrade tokamak, Nuclear Fusion 61 (2) (2020) 024001. doi:10.1088/1741-4326/abc936.
URL https://doi.org/10.1088/1741-4326/abc936

[3] O. Février, C. Theiler, J. R. Harrison, C. K. Tsui, K. Verhaegh, C. Wüthrich, J. A. Boedo,

H. D. Oliveira, B. P. Duval, B. Labit, B. Lipschultz, R. Maurizio, H. Reimerdes, Nitrogen-seeded divertor detachment in TCV L-mode plasmas, Plasma Physics and Controlled Fusion 62 (3) (2020) 035017. doi:10.1088/1361-6587/ab6b00.
URL https://doi.org/10.1088/1361-6587/ab6b00

[4] B. Lipschultz, B. LaBombard, E. Marmar, M. Pickrell, J. Terry, R. Watterson, S. Wolfe, Marfe: an edge plasma phenomenon, Nuclear Fusion 24 (8) (1984) 977. doi:10.1088/0029-5515/24/8/002.
URL https://dx.doi.org/10.1088/0029-5515/24/8/002

[5] J. Wesson, R. Gill, M. Hugon, F. Schüller, J. Snipes, D. Ward, D. Bartlett, D. Campbell, P. Duperrex, A. Edwards, R. Granetz, N. Gottardi, T. Hender, E. Lazzaro, P. Lomas, N. L. Cardozo, K. Mast, M. Nave, N. Salmon, P. Smeulders, P. Thomas, B. Tubbing, M. Turner, A. Weller, Disruptions in JET, Nuclear Fusion 29 (4) (1989) 641. doi:10.1088/0029-5515/29/4/009.
URL https://dx.doi.org/10.1088/0029-5515/29/4/009

[6] J. A. Goetz, C. Kurz, B. LaBombard, B. Lipschultz, A. Niemczewski, G. M. McCracken, J. L. Terry, R. L. Boivin, F. Bombarda, P. Bonoli, C. Fiore, S. Golovato, R. Granetz, M. Greenwald, S. Horne, A. Hubbard, I. Hutchinson, J. Irby, E. Marmar, M. Porkolab, J. Rice, J. Snipes, Y. Takase, R. Watterson, B. Welch, S. Wolfe, C. Christensen, D. Garnier, D. Jablonski, D. Lo, D. Lumma, M. May, A. Mazurenko, R. Nachtrieb, P. O'Shea, J. Reardon, J. Rost, J. Schachter, J. Sorci, P. Stek, M. Umansky, Y. Wang, Comparison of detached and radiative divertor operation in Alcator C-Mod, Physics of Plasmas 3 (5) (1996) 1908–1915. doi:10.1063/1.871986.
URL https://doi.org/10.1063/1.871986

[7] N. Asakura, H. Hosogane, S. Tsuji-Iio, K. Itami, K. Shimizu, M. Shimada, Field reversal effects on divertor plasmas under radiative and detached conditions in JT-60U, Nuclear Fusion 36 (6) (1996) 795. doi:10.1088/0029-5515/36/6/I10.
URL https://dx.doi.org/10.1088/0029-5515/36/6/I10

[8] V. Mertens, M. Kaufmann, J. Neuhauser, J. Schweinzer, J. Stober, K. Buchl, O. Gruber, G. Haas, A. Herrmann, A. Kallenbach, M. Weinlich, High density operation close to Greenwald limit and H mode limit in ASDEX Upgrade, Nuclear Fusion 37 (11) (1997) 1607. doi:10.1088/0029-5515/37/11/I10.
URL https://dx.doi.org/10.1088/0029-5515/37/11/I10

[9] J. Rapp, W. Fundamenski, L. C. Ingesson, S. Jachmich, A. Huber, G. F. Matthews, P. Morgan, M. F. Stamp, J.-E. Contributors, Septum assessment of the JET gas box divertor, Plasma Physics and Controlled Fusion 50 (9) (2008) 095015. doi:10.1088/0741-3335/50/9/095015.
URL https://dx.doi.org/10.1088/0741-3335/50/9/095015

[10] U. Stroth, M. Bernert, D. Brida, M. Cavedon, R. Dux, E. Huett, T. Lunt, O. Pan, M. Wischmeier, the ASDEX Upgrade Team, Model for access and stability of the X-point radiator and the threshold for marfes in tokamak plasmas, Nuclear Fusion 62 (7) (2022) 076008. doi:10.1088/1741-4326/ac613a.
URL https://doi.org/10.1088/1741-4326/ac613a

[11] A. Hatayama, H. Segawa, R. Schneider, D. Coster, N. Hayashi, S. Sakurai, N. Asakura, M. Ogasawara, High Mach flow associated with X-point MARFE and plasma detachment, Nuclear Fusion 40 (12) (2000) 2009. doi:10.1088/0029-5515/40/12/305.
URL https://dx.doi.org/10.1088/0029-5515/40/12/305

[12] V. Kotov, D. Reiter, Formation of a natural X-point multifaceted asymmetric radiation

from the edge in numerical simulations of divertor plasmas, Plasma Physics and Controlled Fusion 54 (8) (2012) 082003. doi:10.1088/0741-3335/54/8/082003.
URL https://dx.doi.org/10.1088/0741-3335/54/8/082003

[13] F. Reimold, M. Wischmeier, M. Bernert, S. Potzel, D. Coster, X. Bonnin, D. Reiter, G. Meisl, A. Kallenbach, L. Aho-Mantila, U. Stroth, Experimental studies and modeling of complete H-mode divertor detachment in ASDEX Upgrade, Journal of Nuclear Materials 463 (2015) 128–134, pLASMA-SURFACE INTERACTIONS 21. doi:https://doi.org/10.1016/j.jnucmat.2014.12.019.
URL https://www.sciencedirect.com/science/article/pii/S002231151400960X

[14] O. Pan, M. Bernert, T. Lunt, M. Cavedon, B. Kurzan, S. Wiesen, M. Wischmeier, U. Stroth, the ASDEX Upgrade Team, SOLPS-ITER simulations of an X-point radiator in the ASDEX Upgrade tokamak, Nuclear Fusion 63 (1) (2022) 016001. doi:10.1088/1741-4326/ac9742.
URL https://dx.doi.org/10.1088/1741-4326/ac9742

[15] R. M. McDermott, R. Dux, T. Pütterich, B. Geiger, A. Kappatou, A. Lebschy, C. Bruhn, M. Cavedon, A. Frank, N. den Harder, E. Viezzer, the ASDEX Upgrade Team, Evaluation of impurity densities from charge exchange recombination spectroscopy measurements at ASDEX Upgrade, Plasma Physics and Controlled Fusion 60 (9) (2018) 095007. doi:10.1088/1361-6587/aad256.
URL https://dx.doi.org/10.1088/1361-6587/aad256

[16] B. Kurzan, A. Lohs, G. Sellmair, M. Sochor, Design and first measurements of the divertor Thomson scattering system on the ASDEX Upgrade tokamak, Journal of Instrumentation 16 (09) (2021) C09012. doi:10.1088/1748-0221/16/09/c09012.
URL https://doi.org/10.1088/1748-0221/16/09/c09012

[17] H. P. Summers, The ADAS User Manual, version 2.6 (2004).
URL http://www.adas.ac.uk

[18] M. Cavedon, B. Kurzan, M. Bernert, D. Brida, R. Dux, M. Griener, S. Henderson, E. Huett, T. Nishizawa, T. Lunt, O. Pan, U. Stroth, M. Wischmeier, E. Wolfrum, the ASDEX Upgrade Team, Experimental investigation of L- and H-mode detachment via the divertor Thomson scattering at ASDEX Upgrade, Nuclear Fusion 62 (6) (2022) 066027. doi:10.1088/1741-4326/ac6071.
URL https://doi.org/10.1088/1741-4326/ac6071

[19] A. Perek, W. A. J. Vijvers, Y. Andrebe, I. G. J. Classen, B. P. Duval, C. Galperti, J. R. Harrison, B. L. Linehan, T. Ravensbergen, K. Verhaegh, M. R. de Baar, MANTIS: A real-time quantitative multispectral imaging system for fusion plasmas, Review of Scientific Instruments 90 (12) (2019) 123514. doi:10.1063/1.5115569.
URL https://doi.org/10.1063/1.5115569

[20] A. Smolders, M. Wensing, S. Carli, H. D. Oliveira, W. Dekeyser, B. P. Duval, O. Février, D. Gahle, L. Martinelli, H. Reimerdes, C. Theiler, K. Verhaegh, the TCV team, Comparison of high density and nitrogen seeded detachment using SOLPS-ITER simulations of the tokamak á configuration variable, Plasma Physics and Controlled Fusion 62 (12) (2020) 125006. doi:10.1088/1361-6587/abbcc5.
URL https://doi.org/10.1088/1361-6587/abbcc5

[21] T. Ravensbergen, M. van Berkel, S. Silburn, J. Harrison, A. Perek, K. Verhaegh, W. Vijvers, C. Theiler, A. Kirk, M. de Baar, the EUROfusion MST1 team, Development of a real-time algorithm for detection of the divertor detachment radiation front using multi-spectral imaging, Nuclear Fusion 60 (6) (2020) 066017. doi:

10.1088/1741-4326/ab8183.
URL https://doi.org/10.1088/1741-4326/ab8183